JOURNAL OF PROPULSION AND POWER
Vol. , No. ,

High-Specific-Impulse Electrostatic Thruster with Argon Propellant

Daisuke Ichihara,* Toshihiro Matsuba,† Akira Iwakawa,‡ and Akihiro Sasoh§
Nagoya University, Nagoya 464-8603, Japan

https://doi.org/10.2514/1.B37675

In this study, an electrostatic thruster was newly developed, in which a diverging magnetic field with a cusp around a cathode was applied by using two solenoid coils. The effects of the magnetic field strength on thrust performance under a similar applied-magnetic-field configuration were investigated. Because of its light weight and lower price, argon was used as a propellant. By increasing the magnetic field strength, the thrust efficiency was improved owing to the suppression of the discharge current while an almost constant thrust was maintained. A specific impulse of 3800 s with thrust efficiency greater than 30% was obtained; the corresponding mass-averaged exhaust velocity exceeded the value by full-potential electrostatic acceleration of singly charged ions. From the thrust performance, ion beam current, and ion energy distribution function that were experimentally measured under the representative operation condition, 32% of the ion beam current and 43% of the total thrust were evaluated as the contribution of doubly charged ions.

Nomenclature

A_{RPA}	=	retarding potential analyzer collection area, m^2
B	=	magnetic field strength, T
e	=	elementary charge, C
F	=	thrust, N
f	=	distribution function
g	=	gravitational acceleration, $\mathrm{m/s}^2$
I_{sp}	=	specific impulse, s
J_c	=	retarding potential analyzer collector current, A
J_d	=	discharge current, A
J_i	=	ion beam current, A
J_k	=	keeper current, A
$\hat{J}_i$	=	propellant utilization efficiency
j_i	=	ion beam current density, $\mathrm{A/m}^2$
K_{iz}	=	ionization rate constant, m^3/s
k	=	Boltzmann constant, $\mathrm{m}^2 \cdot \mathrm{kg}/(\mathrm{s}^2 \cdot \mathrm{K})$
m	=	particle mass, kg
$\dot{m}_a$	=	anode mass flow rate, kg/s
$\dot{m}_c$	=	cathode mass flow rate, kg/s
$\dot{m}_{\mathrm{ent}}$	=	entrainment mass flow rate, kg/s
$\dot{m}_t$	=	$(\equiv \dot{m}_a + \dot{m}_c)$ total mass flow rate, kg/s
n	=	number density, m^{-3}
P	=	$(\equiv J_d V_d + J_k V_k)$ total input power, W
P_n	=	neutral pressure, Pa
R	=	swing arm length, m
r, φ, z	=	cylindrical coordinates
r_a	=	anode radius, m
T	=	temperature, K
u	=	flow velocity, m/s
u_{ex}	=	$(\equiv F/\dot{m}_t)$ exhaust velocity, m/s
V_d	=	discharge voltage, V
V_f	=	floating potential, V
V_k	=	keeper voltage, V
V_{RPA}	=	ion discriminate voltage, V
V_s	=	space potential, V
V_{th}	=	threshold voltage, V
Z	=	charge state
α	=	coefficient
γ	=	secondary electron yield
ε	=	mass-averaged energy, eV
η	=	thrust efficiency
λ_{CEX}	=	mean-free-path of charge exchange collision, m
λ_{iz}	=	mean-free-path of electron impact ionization collision, m
σ_{CEX}	=	cross section of charge exchange collision, m^2
ϕ	=	peak energy of ion energy distribution function, eV
ψ	=	correction factor

Subscripts

e	=	electron
eff	=	effective value
i	=	ion
n	=	neutral
$2+$	=	doubly charged ion
$+$	=	singly charged ion

Received 20 May 2019; revision received 6 October 2019; accepted for publication 4 January 2020; published online XX epubMonth XXXX. Copyright © 2020 by Daisuke Ichihara, Toshihiro Matsuba, Akira Iwakawa, and Akihiro Sasoh. Published by the American Institute of Aeronautics and Astronautics, Inc., with permission. All requests for copying and permission to reprint should be submitted to CCC at www.copyright.com; employ the eISSN 1533-3876 to initiate your request. See also AIAA Rights and Permissions www.aiaa.org/randp.

*Research Associate, Department of Aerospace Engineering.
†Graduate Student, Department of Aerospace Engineering.
‡Lecturer, Department of Aerospace Engineering. Member AIAA.
§Professor, Department of Aerospace Engineering. Associate Fellow AIAA.

I. Introduction

FOR deep-space exploration missions [1] or near-Earth orbit transfers [2], a propulsion system with high exhaust velocity (namely, high specific impulse) is necessary especially in high delta-v missions to enhance the payload ratio. Electric space propulsion options can accelerate ions to an exhaust speed level that is not achievable by chemical propulsion [3]. The typical energy level is in the order of 10^2 eV or higher. Among the electric space propulsions, electrostatic thrusters accelerate ions without collisions, thereby yielding a high thrust efficiency over 50%. In principle, the specific impulse in the electrostatic acceleration is proportional to the square root of V_d/m_i. The typical specific impulse for ion engines, Hall thrusters, cylindrical Hall thrusters, and highly efficient multistage plasma thrusters are 4000 s [4], 1500–3500 s [5], 2000 s [6], and 3000 s [7], respectively. Although these electrostatic thrusters provide high specific impulse with high thrust efficiency, these performances can be achieved only when xenon (Xe) is used as a propellant. Hence, high discharge voltage operation is required to increase specific impulse because xenon has a large atomic mass. Another option to increase specific impulse is the usage of lighter species [8–10] such as argon (Ar). The mass of Ar propellant is about one-third of the Xe propellant. Moreover, Ar cost is much lower than that of Xe cost, 1440 U.S. dollars/kg, which is 240 times higher than the cost of Ar [11]. Because of above advantages, Ar can be an alternative propellant of

Xe. However, many challenges remain in regard to thrust efficiency improvement. Because of its high ionization energy (Ar: 15.8 eV, Xe: 12.1 eV) [12] and small electron-impact ionization cross section (Ar: 41×10^{-18} cm^2, Xe: 207×10^{-18} cm^2 with 20 eV of electron energy) [13], an Ar propellant operation has demonstrated worse thrust performances than the conventional Xe propellant operation. To enhance Ar propellant ionization, Ichihara et al. [14] proposed a diverging-magnetic field electrostatic thruster that comprised a diverging magnetic field between a ring anode that was coaxially set on the center axis and an off-axis hollow cathode in the downstream region. They operated the thruster with an Ar propellant and demonstrated ionization enhancement by the "near-anode ionization scheme." Subsequently, they reported that thrust efficiency competitive to Xe and krypton propellant was obtained even with argon [15]. In Ref. [16], the effects of the magnetic field profile near the anode were investigated. However, they could not vary the magnetic field strength while maintaining the magnetic field configuration because permanent magnets and yokes were used to apply the magnetic field. In this study, we newly developed an electrostatic thruster comprising of two solenoid coils to investigate the effect of magnetic field strength on thrust performance with a similar magnetic field configuration. The thrust performance was related to ion beam characteristics and plasma properties measured using electrostatic probes.

II. Experimental Apparatus

A. Thruster Head

Figure 1 shows the schematics of a diverging-magnetic-field, electrostatic thruster with two solenoid coils. The thruster head comprises a ring anode, a hollow cathode, and two water-cooled-solenoid coils. The ring anode had an inner radius (r_a) of 15 mm, outer radius of 22.5 mm, and an effective length of 10 mm. The ring anode and central ceramic plate made of boron nitride were coaxially set with a clearance of 1.5 mm that served as an annular slit for propellant injection. To apply a slowly diverging magnetic field followed by a cusped region, two solenoid coils (1 and 2) with supplied currents in the opposite direction to each other were used. The inner diameter, outer diameter, and bobbin length of solenoid coil 1 were 60.5, 200, and 80 mm, respectively. The central ceramic plate was set at the center of solenoid coil 1. The inner diameter, outer diameter, and bobbin length of solenoid coil 2 were 216.3, 310, and 40 mm, respectively. The cylindrical coordinates (z, r), where z and r are the axial and radial coordinates, respectively, were defined in the axisymmetric configuration, with their origins at the center of solenoid coil 1. The center of solenoid coil 2 was located at $(z, r) = (60\text{ mm}, 0\text{ mm})$. The axial magnetic field B at $(z, r) = (0\text{ mm}, 0\text{ mm})$ was varied as 100, 150, and 200 mT. The hollow cathode (DLHC-1000, Kaufman and Robinson, Inc.) was located at $(z, r) = (172\text{ mm}, 115\text{ mm})$ in the cusp region, where the magnetic field strength was less than 1 mT.

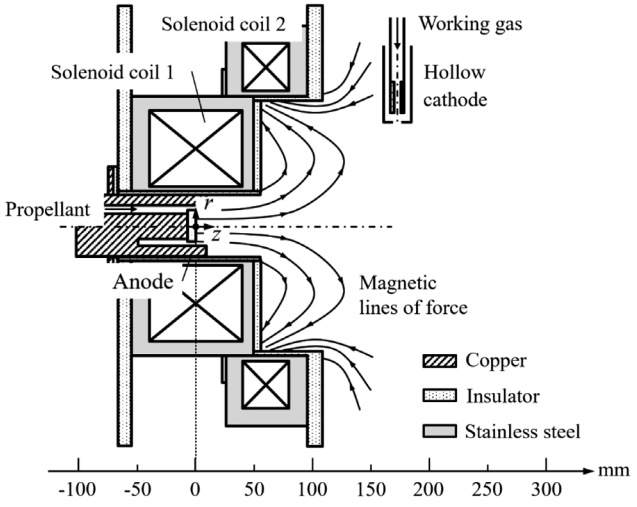

Fig. 1 Schematic of diverging magnetic field–electrostatic thruster.

B. Thrust Measurement and Diagnostics

1. *Thrust Measurement*

A pendulum-type thrust stand of the same type as is described in Ref. [17], consisting of a 1-m-long stand arm, vacuum bellows, and two bearings at the fulcrum, was used to measure the thrust. Figure 2 shows the schematic of the thrust stand with the calibration system used in this study. Cooling water and propellant were fed by copper tubes through the stand arm. The pendulum displacement was amplified by a 1.1-m-long aluminum arm located outside the chamber and was sensed by using a linear variable differential transformer (LVDT1301-2, Shinko Electric Co., Ltd.). The thrust stand was calibrated using an arrangement of weights, a pulley, and a direct-current (DC) motor under the same vacuum conditions as during thruster operations. The details of the calibration procedure were presented in the previous paper [18]. From 0 to 42 mN, a linearity with a regression line of correlation coefficient 0.99 was confirmed. The calibrated conversion factor was 259 ± 3.2 mN/V. The associated uncertainty in the thrust measurement was 1.3% of the minimum thrust level in this study. Although the solenoid coils were water cooled, the displacement signal exhibited a thermal drift while supplying large coil currents. This thermal drift could cause uncertainty in the thrust measurement. To apply 200 mT of magnetic field strength, the maximum thermal drift was introduced and the uncertainty corresponded to 0.8 mN, which was 7.4% of the minimum measured thrust. The effects of electromagnetic force, known as the "tare force," and of the cold flow thrust, that is, the thrust without discharge, were negligible.

2. *Measurement of Ion Beam Current and Energy*

The ion beam current density and ion beam divergence half-angle were measured by a nude Faraday probe [19] that comprised an ion collector and a coaxial guard ring. The details of the probe were described in Ref. [16]. The nude Faraday probe was swept using a stepping motor (PK56, Oriental Motor Co., Ltd.). The rotation center was $(z, r) = (109\text{ mm}, 0\text{ mm})$, and the swing arm length was 250 mm. The swing speed was 180 deg/s. The accuracy of the angular positioning was 0.1 deg. Both the ion collector and guard ring were negatively biased at 27 V with respect to the cathode potential. The ion current flowing into the ion collector was measured as a voltage drop through a 1-kΩ resistor ($\pm 5.0\%$ accuracy). Figure 3 shows an example of the measured ion current density j_i as a function of the azimuthal angle φ. Assuming an axisymmetric exhaust plume, ion current J_i is calculated as in Eq. (1) [20].

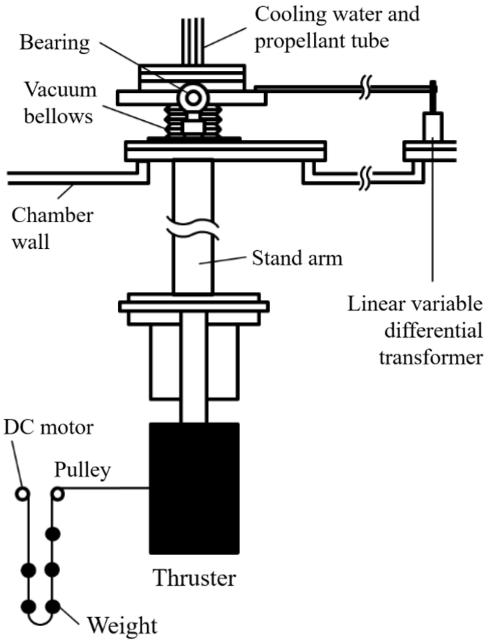

Fig. 2 Schematic of the thrust stand with the calibration system used in this study. More information about the stand is provided in Ref. [18].

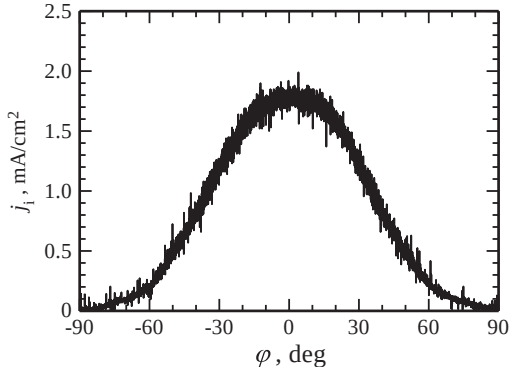

Fig. 3 Example of j_i (φ) distribution, $\dot{m}_a = 0.41$ mg/s, $\dot{m}_c = 0.14$ mg/s, $V_d = 200$ V, $B = 100$ mT.

$$J_i \equiv \int_{\varphi_2}^{\varphi_1} j_i(\varphi)\pi R^2 |\sin\varphi| \mathrm{d}\varphi \tag{1}$$

where R is a swing radius, and φ_1, φ_2 are the swing ranges that are set in two types: $(\varphi_1, \varphi_2) = (-\pi/2, 0)$ and $(0, \pi/2)$, respectively. J_i was evaluated as the average of these two integrations.

The ion energy distribution function f_ε was measured by a retarding potential analyzer (RPA) [21]. The RPA comprised three metal meshes fabricated using stainless steel. The first mesh had a floating potential, the second one was negatively biased by 100 V with respect to the cathode potential to repeal electrons, and the third one had a variable potential, V_{RPA}, from −20 to 350 V with respect to the cathode potential to resolve ion energy. The current reaches that the RPA-ion collector, J_c, was

$$J_c = eA_{\mathrm{RPA}} \int_{u_{\min}}^{\infty} u f_v(u)\, \mathrm{d}u \tag{2}$$

Here, e is an elementary charge, A_{RPA} is collection area of ion current, u is ion velocity, $u_{\min}$ is minimum ion velocity to reach the ion collector, and f_v is ion velocity distribution function. Based on the relation that $V_{\mathrm{RPA}} = m_i u^2/(2e)$, where m_i is ion mass, the differentiation of J_c with respect to V_{RPA} was described as

$$\frac{dJ_c}{dV_{\mathrm{RPA}}} = \frac{e^2 A_{\mathrm{eff}}}{m_i} f_v\left(\sqrt{\frac{2eV_{\mathrm{RPA}}}{m_i}}\right) \tag{3}$$

The f_ε (V_{RPA}) was calculated as $f_\varepsilon = f_v(u)/(m_i u)$ [22]. The details of the RPA and data analysis procedures have been described in our previous study [16]. Figure 4 shows an example of J_c and associated f_ε. The ion current was normalized by the averaged ion current in $V_{\mathrm{RPA}} < 0$ V. As shown in Fig. 4, the f_ε contains three peaks. The first peak energy (ϕ_s) corresponds to thermalized ions ejected from the hollow cathode; the second (ϕ_1) and third peak energies (ϕ_2) correspond to the kinetic energies of electrostatically accelerated ions. Note here that, in the f_ε, we do not resolve contributions of singly and doubly ionized ions.

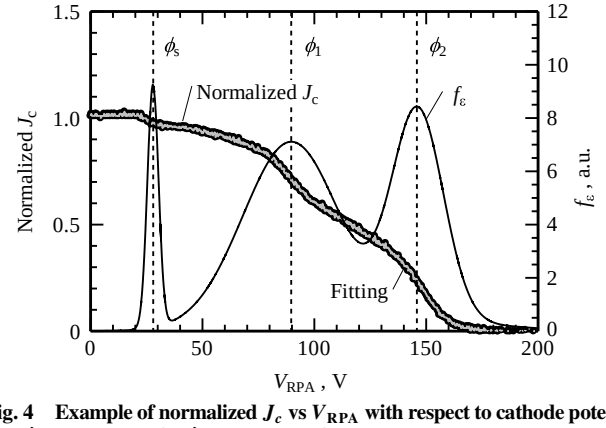

Fig. 4 Example of normalized J_c vs V_{RPA} with respect to cathode potential, $\dot{m}_a = 0.41$ mg/s, $\dot{m}_c = 0.14$ mg/s, $V_d = 150$ V, $B = 100$ mT. The f_ε curve was fit to the sum of three Gaussian curves by the least-square method.

3. *Plasma Diagnostics*

A double, cylindrical probe was used for electron number density, n_e, and electron temperature, T_e, measurements. The tungsten-made probe tip had a diameter of 0.3 mm and effective length of 3.0 mm. The distance between the two wires was set to 2.2 mm. The bias voltage applied at the two wires was varied from −150 to 150 V in 10 Hz using a bipolar power supply (EC1000SA, NF Corp.). The double probe current was measured from the potential drop at the 150-Ω resistor connected to the probe circuit in series. Furthermore, n_e and T_e were calculated based on the fitting parameters of the thin sheath theory with sheath expansion correction [23]. The uncertainties of n_e and T_e were up to $+13\%/-16\%$ and $\pm 15\%$, respectively.

An emissive probe was used for floating potential, V_f, measurement. The emission part was fabricated using a 1% thoriated tungsten wire. The wire diameter was 0.203 mm and the bend radius was 1.1 mm. To emit sufficient amount of electrons, the emission part was Joule heated by supplying 4.5 A of constant heater current. To estimate space potential, V_s, the measured V_f was corrected by T_e as

$$V_s = V_f + \Psi kT_e/e \tag{4}$$

Here, k is Boltzmann constant. The correction factor Ψ depends on the Debye length ratio to the wire radius [24]. The uncertainty of V_s was of the same order as of T_e. Considering the voltage drop at the emission part, the uncertainty in V_s was $+0.15\Psi(kT_e/e)/-0.9\Psi(kT_e/e) \pm 3.0$ V.

The double probe and emissive probe were swept using the same stepping motor as those used in the $j_i(\varphi)$ measurement with a sweep time shorter than 0.2 s at each point. The probe measurement position interval was 5 mm at the least in the axial direction, and 5–20 mm in the radial direction. For the r- and z-axis motion movements, electrical actuators XA-50L-400 and XA-42L-200 (both made by SUS Corporation) were used. The position resolution was ±1 mm.

C. Vacuum Facility and Supplying Equipment

All experiments were conducted in a stainless-steel vacuum chamber with a diameter of 2.0 m and a length of 4.0 m. The vacuum chamber was evacuated using a turbo molecular pump (3203LMC, SHIMADZU Corp.) with an exhaust speed of 3200 L/s and was backed by a rotary pump (2100D, adixen Vacuum Products) with an exhaust speed of 33.3 L/s. The background pressure inside the camber was monitored by an ionization gauge (GI-TL3, ULVAC, Inc.). The base pressure of the system was less than 1×10^{-3} Pa ($= 7.5 \times 10^{-3}$ torr) and, during operation with an argon flow of 0.55–0.97 mg/s, the background pressure remained in low-to-middle 10^{-2} Pa ($= 7.5 \times 10^{-2}$ torr) range.

The effects of the background pressure in the vacuum chamber on the thrust performance were evaluated based on the entrainment flow rate (random mass-flux flowing into the acceleration channel). Assuming that the residual gas in the chamber was thermalized, the entrainment mass flow rate, $\dot{m}_{\mathrm{ent}}$, was given by

$$\dot{m}_{\mathrm{ent}} = \frac{1}{4} m_n n_n u_n \times \pi r_a^2 \tag{5}$$

where m_n is mass of the neutral particle, $u_n = (8kT_n/[\pi m_n])^{1/2}$ is thermal velocity of the neutral particle, P_n is background pressure, and $n_n = P_n/(kT_n)$ is neutral number density. Supplying 0.41 mg/s of anode mass-flow rate, $\dot{m}_a$, and 0.14 mg/s of cathode mass-flow rate, $\dot{m}_c$, the P_n was 13 mPa and $n_n = 3.1 \times 10^{18}$ m^{-3} with assuming neutral temperature T_n of 300 K. In this operating condition, $\dot{m}_{\mathrm{ent}} = 1.5 \times 10^{-2}$ mg/s, which was 3.6% of $\dot{m}_a$ and smaller than the uncertainty in the mass flow controller. The charge exchange

(CEX) collision is also important to estimate the background pressure effect on the ion property measurements. Assuming that fast ions collide with slow atoms, the mean-free path of the CEX collision, λ_{CEX}, is

$$\lambda_{\mathrm{CEX}} = \frac{1}{n_n \sigma_{\mathrm{CEX}}} \tag{6}$$

When singly and doubly charged ions collide with neutral atoms, the cross section of the CEX collision, σ_{CEX}, for 10^2 eV of ion energy and the calculated λ_{CEX} are summarized in Table 1. The calculated λ_{CEX} was comparable or longer than the chamber radius. However, inside the discharge channel, n_n should be evaluated as $n_n = \dot{m}_a/(m_i u_n \pi r_a^2) = 2.2 \times 10^{19}$ m^{-3}, which is 10 times higher, and therefore λ_{CEX} can be one-tenth than those of the outside discharge channel. Under this condition, CEX collisions can affect the J_i measurement and can be a one possible process to generate Ar^{2+}. Beyond the neutral entrainment and CEX collisions, it is well known that thrust also depends on background pressure. Snyder et al. [25] reported the effect of background pressure on thrust measurement that as decreasing background pressure, thrust was decreased. In 0.1 mPa of background pressure operation, obtained thrust was 8% smaller than that of 5 mPa operation. Therefore, it is noted that the presented thrust data can be overestimated in the same level.

Commercially available power supplies and mass flow controllers were used for all experiments. DC power supply was used for the primary discharge power (HX01000-12M2I, Takasago Ltd.), for the hollow cathode (KC8002, Kaufman & Robinson Inc.), and for solenoid coils (N8761A, Agilent Technologies Inc.). The primary power supplies were operated with a constant voltage mode. The uncertainty of the applied voltage was ± 2 V. Meanwhile, the hollow cathode power supply was operated at a constant current mode. Argon gas (99.9999% of purity) was supplied through a mass flow controller (3660 SERIES, Kojima Instruments, Inc.) with an uncertainty of $\pm 6.2 \times 10^{-2}$ mg/s.

III. Experimental Results and Discussion

A. Operating Conditions

The operating conditions are summarized in Table 2. The uncertainties in B and discharge current J_d were ± 10 mT and ± 51 mA, respectively. The keeper current J_k was fix at 2.0 A. In this experiment, discharge voltage V_d was varied from 125 to 250 V and total input power, including power consumption in the hollow cathode $P(= J_d V_d + J_k V_k)$, ranged from 550 to 2330 W. Each operating condition was repeated at least three times. In the following figures and tables, symbols indicate the averaged value for each operating condition. The error bars in thrust F and J_d represent the standard deviation ($\pm\sigma$) obtained after a number of trials, whereas the uncertainties in J_i correspond to the uncertainty in the averaging.

B. Thrust and Discharge Current Characteristics

Figure 5 shows the $\dot{m}_a$ dependence of F and J_d with different B and a constant V_d of 200 V. Regardless of B, F, and J_d increased with increasing $\dot{m}_a$. For instance, with $B = 150$ mT, F increased from 13 to 33 mN, whereas J_d increased from 3.4 to 9.6 A. With a constant $\dot{m}_a$, F did not show B dependence, whereas J_d decreased with increasing B. With $\dot{m}_a = 0.62$ mg/s, J_d decreased from 7.0 to 5.7 A as B increased from 100 to 200 mT. Even for $B = 200$ mT, J_d was ~3.8 times higher than the Ampere-equivalent anode flow rate, $e\dot{m}_a/m_i$. Because strengthening the magnetic field suppressed the electron transport across the magnetic field, the electron current from the hollow cathode decreased.

Table 1 σ_{CEX} and calculated λ_{CEX} from Eq. (6) for different CEX processes with $P_n = 13$ mPa (measured) and $T_n = 300$ K (assumed)

Process	σ_{CEX}, m^2	λ_{CEX}, m
$Ar^+_{(\mathrm{fast})} + Ar_{(\mathrm{slow})} \rightarrow Ar^+_{(\mathrm{slow})} + Ar_{(\mathrm{fast})}$	3.7×10^{-19} [26]	0.85
$Ar^{2+}_{(\mathrm{fast})} + Ar_{(\mathrm{slow})} \rightarrow Ar^{2+}_{(\mathrm{slow})} + Ar_{(\mathrm{fast})}$	1.7×10^{-19} [27]	1.9
$Ar^{2+}_{(\mathrm{fast})} + Ar_{(\mathrm{slow})} \rightarrow Ar^+_{(\mathrm{slow})} + Ar^+_{(\mathrm{fast})}$	2.2×10^{-21} [27]	52

Table 2 Operating conditions

Symbol	Unit	Setting
$\dot{m}_a$	mg/s	0.41–0.83
$\dot{m}_c$	mg/s	0.14
$\dot{m}_t$	mg/s	0.55–0.97
V_d	V	125–250
P	W	550–2330
B	mT	100–200
J_k	A	2.0

Figure 6 shows the V_d dependence of F and J_d with different B and a constant $\dot{m}_a$ of 0.41 mg/s. Both F and J_d increased gradually with V_d. Along with the $\dot{m}_a$ dependence, F indicated a slight dependence on B while J_d decreased with increasing B. Particularly for $B = 200$ mT, $J_d = 3.5$ A, which was 3.5 times as large as $e\dot{m}_a/m_i$. For $B = 200$ mT, V_d could not be decreased to less than 225 V owing to ignition failure.

In an electrostatic acceleration, the characteristic ion energy of a singly charged ion, ε, is expressed by

$$\varepsilon \equiv \frac{1}{2e} m_i u_{\mathrm{ex}}^2 = \alpha (V_d - V_{\mathrm{th}}) \tag{7}$$

Here, $u_{\mathrm{ex}} = F/\dot{m}_t$ is a mass-averaged exhaust velocity, $\dot{m}_t + \dot{m}_a + \dot{m}_c$ is a total mass-flow rate, α is a coefficient, and V_{th} is a threshold voltage to generate thrust. For an ideal electrostatic acceleration of singly charged ion, $\alpha = 1$ and $V_{\mathrm{th}} = 0$. Figure 7 shows the experimentally measured V_d dependence of ε with different $\dot{m}_a$. The ε performances were fit to Eq. (7) with α exceeding unity. As will be discussed in detail later, α exceeding unity suggests contribution of multiple charged ions. The threshold voltage V_{th} to generate thrust was estimated as a fitting parameter. In $V_d \leqq V_{\mathrm{th}}$ operation, the applied voltage was consumed only to generate ions, whereas for $V_d > V_{\mathrm{th}}$, the applied voltage was used for ion

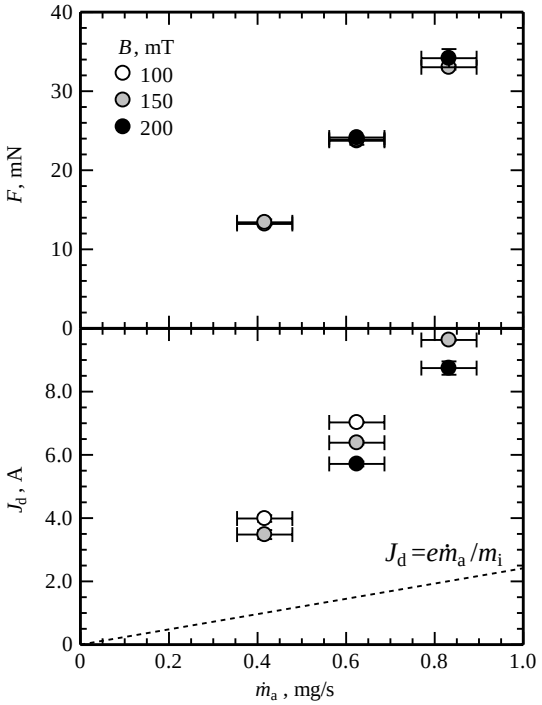

Fig. 5 $\dot{m}_a$ dependence of F and J_d with different B, $\dot{m}_c = 0.14$ mg/s, $V_d = 200$ V.

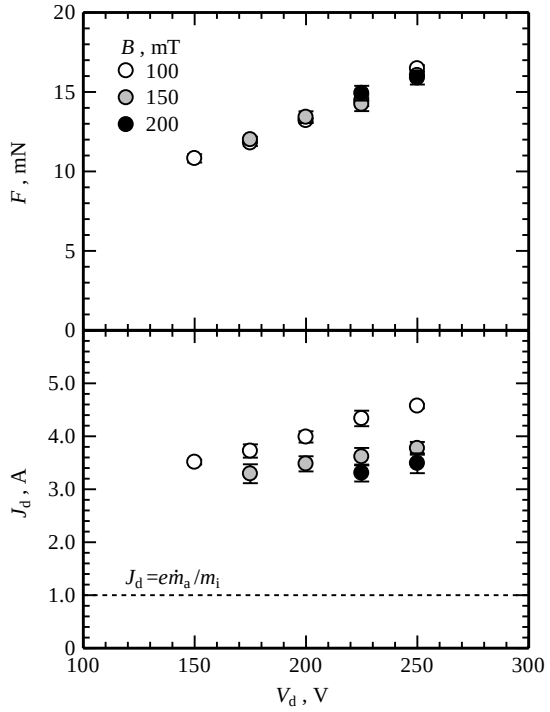

Fig. 6 V_d dependence of F and J_d with different B, $\dot{m}_a = 0.41$ mg/s, $\dot{m}_c = 0.14$ mg/s.

acceleration. The V_{th} values were 81±4.7 V for $\dot{m}_a = 0.41$ mg/s, and 70 ± 2.4 V for 0.62 and 0.83 mg/s operations.

The specific impulse I_{sp} and thrust efficiency η were calculated as follows:

$$I_{sp} \equiv \frac{F}{\dot{m}_t g} \tag{8}$$

$$\eta \equiv \frac{F^2}{2\dot{m}_t P} \tag{9}$$

Here, g is the gravitational acceleration. Given the uncertainties in F, $\dot{m}_t$, J_d, V_d, J_k, and keeper voltage V_k, the maximum relative uncertainty of I_{sp} and η was calculated as ±7.9 and ±14%, respectively, based on the low propagation of error. Figure 8 shows the I_{sp} and η with different B. Overall, η increased with I_{sp}. The thrust–power ratio, F/P, ranged from 13 to 22 mN/kW. As shown in Figs. 5 and 6, because the strengthening magnetic field suppressed J_d while exhibiting no effects on F, η increased with B. The maximum η was 33% with 3550 s of I_{sp}. The maximum I_{sp} was 3890 s with $\dot{m}_a = 0.83$ mg/s, $V_d = 250$ V, and $B = 200$ mT.

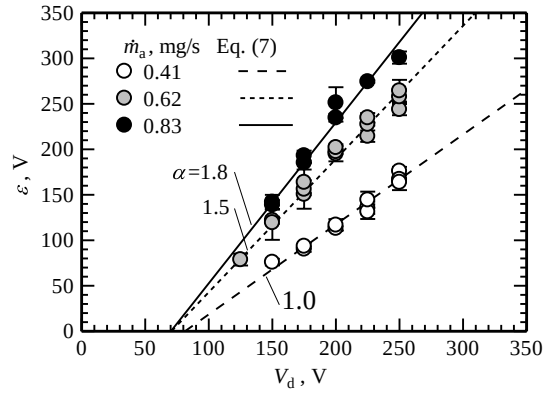

Fig. 7 V_d dependence of ε with different $\dot{m}_a$. Operating conditions are summarized in Table 2.

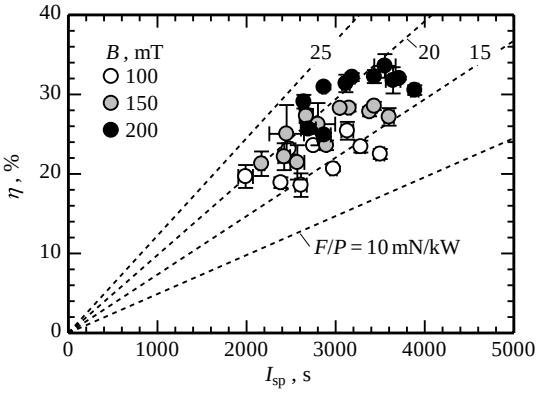

Fig. 8 Thrust performance with different B. Operating conditions are summarized in Table 2.

Compared with previous Ar propellant operations in Hall thrusters [26–28], both the obtained I_{sp} and η were higher than those of previous reports. Although V_d was up to 250 V, the maximum I_{sp} was higher than that of conventional Xe-Hall thrusters even with a 1.0-kV discharge voltage operation [5]. However, compared with the typical η value in the Xe-Hall thruster (~50%), presented η (~33%) was still at a lower level. Note here that the thrust performance shown in Fig. 8 was evaluated by using $\dot{m}_t$, in which $\dot{m}_c$ that is necessary only for the hollow cathode operation was included. Considering that $\dot{m}_c$ had a fraction of 15–26% in $\dot{m}_t$, the effective thrust performance would be even higher than the present evaluation.

C. Ion Beam Characteristics

Figure 9 shows the calculated $f_\varepsilon(V_{RPA})$ variations with different V_d. As mentioned in Sec. II, the f_ε contains three peaks, which are summarized in Table 3.

With all V_d, the value of ϕ_s remained at around 30 V. The kinetic energies of the accelerated ions should correspond to ϕ_1 and ϕ_2. With increasing V_d, ϕ_1 increased a little and ϕ_2 stayed almost at V_d. These multipeak ion energy distribution functions have been observed in

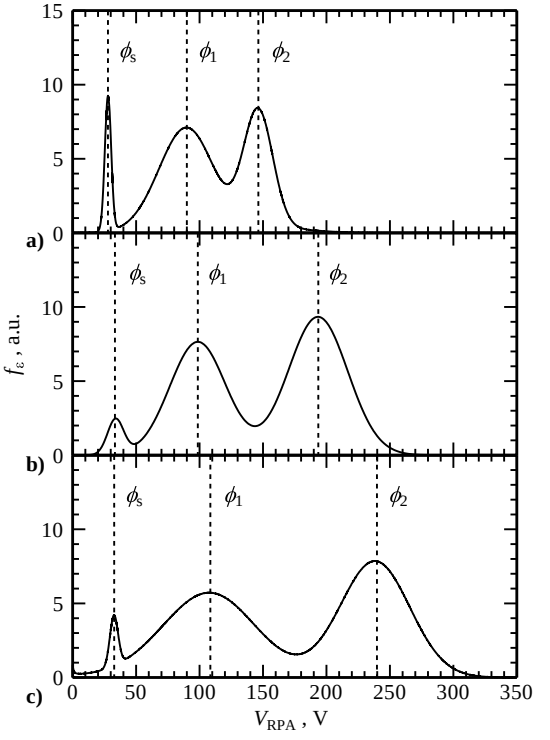

Fig. 9 Ion energy distribution function with a) $V_d = 150$ V, b) $V_d = 200$ V, and c) $V_d = 250$ V, $\dot{m}_a = 0.41$ mg/s, $\dot{m}_c = 0.14$ mg/s, $B = 100$ mT.

Table 3 Peak energies of f_ε, $\dot{m}_a = 0.41$ mg/s, $\dot{m}_c = 0.14$ mg/s, $B = 100$ mT

V_d, V	ϕ_s, V	ϕ_1, V	ϕ_2, V
150	28	90	146
200	33	99	194
250	33	108	240

helicon discharge plasmas [29]. It was reported that a higher energy peak corresponded to energetic ions without collisions and a lower energy peak corresponded to CEX-made thermalized ions. Another possibility is the existence of plural ionization regions [30]. The peak energy depends on the electric potential where the ions were generated. The two-peak characteristics suggest the existence of two ionization regions in the discharge channel. The relation between the ionization regions and the space potential is discussed in the next section.

Table 4 summarizes the V_d dependence of $\hat{J}_i(\equiv J_i/[e\dot{m}_t/m_i])$ with different $\dot{m}_a$. For a singly charged ion, the value $\hat{J}_i$ represents the propellant utilization efficiency. For both $\dot{m}_a$, $\hat{J}_i$ increased with increasing V_d. At $V_d = 250$ V, $\hat{J}_i = 2.1$ and 2.9 for $\dot{m}_a = 0.41$ and 0.62 mg/s, respectively. The ionization frequency is proportional to the product of the neutral atom number density and the electron number density, the latter of which is increased also with increasing $\dot{m}_a$; the larger the $\dot{m}_a$, the higher the $\hat{J}_i$ becomes. Because the secondary electron yield γ depends on the charge state of the incident ion, the fractions of singly and multiple charged ions in J_i are necessary for correcting the effects of secondary electron emission. Here, we estimated the upper and lower limits of $\hat{J}_i$. Assuming that the extracted ions comprised only singly or doubly charged ions, $\hat{J}_i$ should be divided by $(1+\gamma^+)$ or $(1+\gamma^{2+})$ for singly and doubly charged ions, respectively. Here corrected $\hat{J}_i$ for singly and doubly charged ions were described as $\hat{J}_i^+(\equiv\hat{J}_i/[1+\gamma^+])$ and $\hat{J}_i^{2+}(\equiv\hat{J}_i/[1+\gamma^{2+}])$, respectively. The estimated values of $\hat{J}_i^+$ and $\hat{J}_i^{2+}$ are also summarized in Table 4. The values of γ^+ and γ^{2+} are given by Ref. [31]. All of $\hat{J}_i^+$ were higher than 1.0; however, $\hat{J}_i^{2+}$ were lower than 2.0. Hence, the extracted ion beam comprised singly and doubly charged ions.

Based on the ion beam characteristics, the mass flow rates of the singly and multiple charged ions were estimated. Assume that the extracted ion beam comprises only singly and doubly charged ions, and that each charge-state ion can exhibit a beam energy of both ϕ_1 and ϕ_2 (potential equivalent) with probability $f_\varepsilon(\phi_1)$ and $f_\varepsilon(\phi_2)$, respectively. Hence, four types of ions exist: 1) singly charged ions with kinetic energy ϕ_1, 2) singly charged ions with kinetic energy ϕ_2, 3) doubly charged ions with kinetic energy ϕ_1, and 4) doubly charged ions with kinetic energy ϕ_2. The mass flow rates of each charge state/kinetic energy ion are designated as $\dot{m}_1^+$, $\dot{m}_2^+$, $\dot{m}_1^{2+}$, and $\dot{m}_2^{2+}$, respectively. Under these assumptions, the mass, charge, and momentum conservation equations are given by

$$\dot{m}_a + \dot{m}_c = \dot{m}_1^+ + \dot{m}_2^+ + \dot{m}_1^{2+} + \dot{m}_2^{2+} \tag{10}$$

Table 4 V_d dependence of $\hat{J}_i$ with different $\dot{m}_a$, $\dot{m}_c = 0.14$ mg/s, $B = 100$ mT

$\dot{m}_a$, mg/s	V_d, V	$\hat{J}_i^+$	$\hat{J}_i^+$	$\hat{J}_i^{2+}$
0.41	150	1.6 ± 0.3	1.4 ± 0.2	1.0 ± 0.2
	200	1.7 ± 0.3	1.6 ± 0.3	1.1 ± 0.2
	250	2.1 ± 0.3	2.0 ± 0.3	1.4 ± 0.2
0.62	150	2.0 ± 0.2	1.7 ± 0.2	1.3 ± 0.2
	200	2.3 ± 0.3	2.1 ± 0.3	1.5 ± 0.2
	250	2.9 ± 0.3	2.6 ± 0.3	1.9 ± 0.2

Corrected values for singly charged ions $\hat{J}_i^+$ and doubly charged ions $\hat{J}_i^{2+}$ are also summarized.

$$J_i = (1+\gamma^+)(e\dot{m}_1^+/m_i + e\dot{m}_2^+/m_i) + (1+\gamma^{2+})(2e\dot{m}_1^{2+}/m_i + 2e\dot{m}_2^{2+}/m_i) \tag{11}$$

$$F = (\dot{m}_1^+ u_1^+ + \dot{m}_2^+ u_2^+ + \dot{m}_1^{2+} u_1^{2+} + \dot{m}_2^{2+} u_2^{2+})\langle\cos\varphi\rangle \tag{12}$$

Here, we assumed that each ion has the same beam divergence half-angle, $\langle\cos\varphi\rangle$. The velocities of each charge state/kinetic energy ion, u_1^+, u_2^+, u_1^{2+}, and u_2^{2+}, were evaluated by assuming full utilization of the acceleration potential, that is, $u = (2eZ\varphi/m_i)^{1/2}$; the $\langle\cos\varphi\rangle$ was calculated from [20]

$$\langle\cos\varphi\rangle \equiv \int_{\varphi_2}^{\varphi_1} j_i(\varphi)|\sin\varphi|\cos\varphi\,\mathrm{d}\varphi \Big/ \int_{\varphi_2}^{\varphi_1} j_i(\varphi)|\sin\varphi|\,\mathrm{d}\varphi \tag{13}$$

$\langle\cos\varphi\rangle$ was evaluated as the average value after setting $(\phi_1, \phi_2) = (-\pi/2, 0)$ and $(0, \pi/2)$ in Eq. (13). The peak value ratio of f_ε was related to the ion number density ratio [22].

$$f_\varepsilon(\phi_1) : f_\varepsilon(\phi_2) = \dot{m}_1^+/u_1^+ + \dot{m}_1^{2+}/u_1^{2+} : \dot{m}_2^+/u_2^+ + \dot{m}_2^{2+}/u_2^{2+} \tag{14}$$

By substituting the operating parameters $(\dot{m}_a, \dot{m}_c)$ and measured parameters $(J_i,\ F,\ \langle\cos\varphi\rangle,\ \phi,\ \phi_2,\ f_\varepsilon(\phi_1)$ and $f_\varepsilon[\phi_2])$ with $V_d = 200$ V and $B = 100$ mT, each ion mass flow rate was calculated using Eqs. (10–14). Figure 10a shows the calculated mass flow rates of each charge state/kinetic energy ion. The extracted ion beam comprised 0.38 mg/s of singly charged ions, which were 68% of $\dot{m}_t$ and the remaining were the doubly charged ions. Among the doubly charged ions, 87.5% of the ions had a kinetic energy of ϕ_2. The thrust components from the singly and doubly charged ions are also shown in Fig. 10b. The thrust components were calculated as $F = \dot{m}u\langle\cos\varphi\rangle$. The dominant thrust component originated from the singly charged ions. The thrust from the singly charged ions was 7.6 mN, which was 57% of the measured F. The doubly charged ions with kinetic energy ϕ_2 generated 5.1 mN of thrust, which was 39% of the total measured thrust. Compared with the singly charged ions, the exhaust velocity of the doubly charged ions can be $2^{1/2}$ times faster. By accelerating the doubly charged ions using a full potential difference between the anode and cathode, a high-specific-impulse operation was realized.

D. Plasma Diagnostics

Figure 11 shows the V_s, n_e, and T_e distributions with $\dot{m}_a$ $\dot{m}_a = 0.41$ mg/s, $\dot{m}_c = 0.14$ mg/s, $V_d = 200$ V, and $B = 100$ mT. In $z \le 30$ mm, V_s remained at the same potential as the applied voltage of 200 V even on the thruster central axis. From $z > 30$ mm, V_s started to decrease monotonically toward the downstream region. As shown in Fig. 11b, n_e remained in the order of 10^{17} m^{-3} throughout the investigated region. In our previous report [16], n_e indicated a local peak value (up to 10^{20} m^{-3}) at the vicinity of the anode where the magnetic field was applied by using the

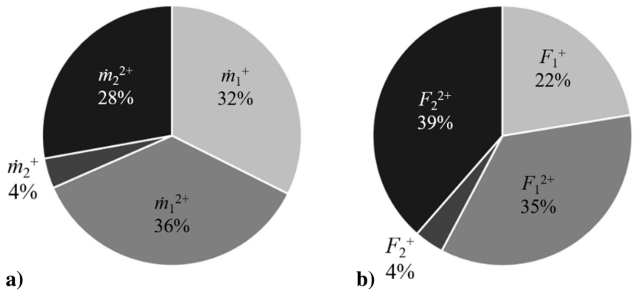

Fig. 10 Calculated a) mass flow rate and b) thrust component of each charge state/kinetic energy ion, $\dot{m}_a = 0.41$ mg/s, $\dot{m}_c = 0.14$ mg/s, $V_d = 200$ V, $B = 100$ mT.

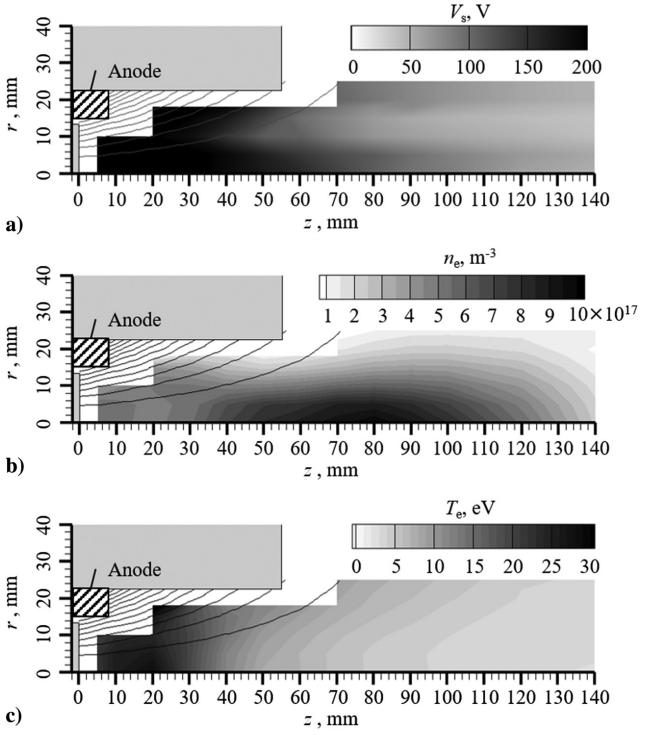

Fig. 11 a) Space potential V_s, V; b) electron number density n_e, m^{-3}; and c) electron temperature T_e, eV distributions, $\dot{m}_a = 0.41$ mg/s, $\dot{m}_c = 0.14$ mg/s, $V_d = 200$ V, $B = 100$ mT. The double probe measured n_e and T_e. V_s was calculated by Eq. (4) based on V_f measurement by the emissive probe. The linear interpolation scheme was used for data smoothing.

permanent magnet turned from the axial to radial components; such a high number density peak irrelevant to the applied magnetic field pattern was not observed. Meanwhile, at $(z, r) = (80\text{ mm}, 0\text{ mm})$, n_e reached the maximum value of 9.9×10^{17} m^{-3}. At this position, $V_s = 110$ V, which was close to the ϕ_1 value ($= 96$ V). The T_e distribution exhibited a local peak value of 28 eV at $(z, r) = (20\text{ mm}, 0\text{ mm})$. In $z \leqq 20$ mm, T_e remained higher than 20 eV and then quickly decreased to the downstream region. From n_e and T_e distributions, the mean free path of the electron-impact ionization processes λ_{iz} was estimated from $\lambda_{\text{iz}} = u_n/(n_e K_{\text{iz}})$. Here, K_{iz} is an ionization rate constant as a function of T_e. The three ionization processes as summarized in Table 5 were taken into account. Here, we assumed $T_n = 300$ K and then $u_n = 398$ m/s. Using n_e and T_e values at $(z, r) = (20\text{ mm}, 0\text{ mm})$, that is, $n_e = 4.8 \times 10^{17}$ m^{-3} and $T_e = 28$ eV, K_{iz} of each ionization processes was calculated from Ref. [32]. Because λ_{iz} of process 3 is longer than the length of discharge region, Ar^{2+} can be generated by a stepwise ionization process, 1 and 2, and the effective ionization mean free path of generating Ar^{2+} was 50 mm. Because the electrostatic acceleration is a collisionless process, the ion kinetic energy depends only on the electric potential where the ion was generated. From potential measurements, V_s at $(z, r) = (50\text{ mm}, 0\text{ mm})$ was 191 V, which was close to the discharge voltage of 200 V. Therefore, generated Ar^{2+} was electrostatically accelerated by using the almost full potential difference between the anode and cathode.

Table 5 K_{iz} and calculated λ_{iz} for different ionization processes

No.	Process	K_{iz}, m^3/s	λ_{iz}, mm
1	$Ar + e^- \rightarrow Ar^+ + 2e^-$	6.4×10^{-14}	13
2	$Ar^+ + e^- \rightarrow Ar^{2+} + 2e^-$	2.3×10^{-14}	37
3	$Ar + e^- \rightarrow Ar^{2+} + 3e^-$	2.7×10^{-15}	307

IV. Conclusions

In this study, an electrostatic thruster comprising two solenoid coils to apply a diverging magnetic field was newly developed. Using argon as a propellant, the effect of magnetic field strength on thrust performances under an identical magnetic field configuration was investigated. As the magnetic field strength increased, the discharge current was suppressed while the thrust remained almost constant. Owing to discharge current suppression, the thrust efficiency and specific impulse increased with the magnetic field strength. The maximum specific impulse was 3800 s with more than 30% thrust efficiency. The extracted ion beam current was 2–3 times higher than the injected propellant flow rate evaluated on singly charged bases. This large ion beam current indicated that the extracted ion beam contained both singly and multiple charged ions. The ion beam energy distribution function exhibited two different peaks of accelerated ions at different kinetic energies: one was close to the discharge voltage, and the other was at ∼100 eV. Overall, the space potential decreased monotonically from upstream to downstream. The space potential remained at the same level as the discharge voltage until 30 mm away from the discharge channel entrance. Under the experimental environment in this study, doubly charged ions can be generated by CEX collisions inside the discharge channel and/or electron-impact-ionization collisions. The fraction of doubly charged ions was estimated based on the thrust, ion beam current, and ion beam energy distribution function measurements. The ion beam comprised 32% of doubly charged ions, and these ions generated 43% of the total thrust. Because the applied voltage (125–250 V) was significantly higher than the ionization potential of the singly (15.8 eV) and doubly charged ions (27.6 eV), the ionization cost of the multiple charged ions was relatively small. By accelerating the multiple charged ions using a full potential difference between the anode and cathode, a high-specific-impulse operation in a diverging magnetic field was realized.

Acknowledgments

This research was supported by the Japan Society for the Promotion of Science KAKENHI Grant No. 18H03813. The authors thank A. Saito and Y. Nakanishi at the Technical Division, Nagoya University, for their valuable technical assistance.

References

[1] Oh, D. Y., Snyder, J. S., Goebel, D. M., Hofer, R. R., and Randolph, T. M., "Solar Electric Propulsion for Discovery-Class Missions," *Journal of Spacecraft and Rockets*, Vol. 51, No. 6, 2014, pp. 1822–1835. https://doi.org/10.2514/1.A32889

[2] Rathsman, P., Kugelberg, J., Bodin, P., Racca, G. D., Foing, B., and Stagnaro, L., "SMART1: Development and Lessons Learnt," *Acta Astronautica*, Vol. 57, Nos. 2–8, May 2005, pp. 455–468. https://doi.org/10.1016/j.actaastro.2005.03.041

[3] Mazouffre, S., "Electric Propulsion for Satellites and Spacecraft: Established Technologies and Novel Approaches," *Plasma Sources Science and Technology*, Vol. 25, No. 3, 2016, Paper 033002. https://doi.org/10.1088/0963-0252/25/3/033002

[4] Snyder, J. S., Goebel, D. M., Hofer, R. R., and Polk, J. E., "Performance Evaluation of the T6 Ion Engine," *Journal of Propulsion and Power*, Vol. 28, No. 2, 2012, pp. 371–379. https://doi.org/10.2514/1.B34173

[5] Hofer, R. R., Jankovsky, R. S., and Gallimore, A. D., "High-Specific Impulse Hall Thrusters, Part 1: Influence of Current Density and Magnetic Field," *Journal of Propulsion and Power*, Vol. 22, No. 4, 2006, pp. 721–731. https://doi.org/10.2514/1.15952

[6] Kim, H., Lim, Y., Hhoe, W., and Seon, J., "Effect of Multiply Charged Ions on the Performance and Beam Characteristics in Annular and Cylindrical Type Hall Thruster Plasmas," *Applied Physics Letters*, Vol. 105, No. 14, 2014, Paper 144104. https://doi.org/10.1063/1.4897948

[7] Reijen, B., van Lazurenko, A., Weis, S., Heidemann, R., Jaderspeck, J., Genovese, A., Holtmann, P., Ruf, K., and Püttmann, N., "Scalability of the HEMP-T Technology for Station Keeping and Orbit Rising," *34th International Electric Propulsion Conference*, Paper IEPC-2015-344, 2015.

[8] Linnell, J. A., and Gallimore, A. D., "Efficiency Analysis of a Hall Thruster Operating with Krypton and Xenon," *Journal of Propulsion and Power*, Vol. 22, No. 6, 2006, pp. 1402–1418. https://doi.org/10.2514/1.19613

[9] Szabo, J., Pote, B., Paintal, S., Robin, M., Hillier, A., Branam, D. R., and Huffman, R. E., "Performance Evaluation of an Iodine-Vapor Hall Thruster," *Journal of Propulsion and Power*, Vol. 28, No. 4, 2012, pp. 848–857. https://doi.org/10.2514/1.B34291

[10] Hopkins, M. A., and King, L. B., "Performance Comparison Between a Magnesium- and Xenon-Fueled 2 Kilowatt Hall Thruster," *Journal of Propulsion and Power*, Vol. 32, No. 4, 2016, pp. 1015–1021. https://doi.org/10.2514/1.B35731

[11] Kieckhafer, A., and King, L. B., "Energetics of Propellant Options for High-Power Hall Thrusters," *Journal of Propulsion and Power*, Vol. 23, No. 1, 2007, pp. 21–26. https://doi.org/10.2514/1.16376

[12] Gstir, B., Denifl, S., Hanel, G., Rümmele, M., Fiegele, T., Cicman, P., Stano, M., Matejcik, S., Scheier, P., Becker, K., Stamatovic, A., and Märk, T. D., "Electron Impact Multiple Ionization of Neon, Argon and Xenon Atoms Close to Threshold: Appearance Energies and Wannier Exponents," *Journal of Physics B: Atomic, Molecular and Optical Physics*, Vol. 35, No. 13, 2002, pp. 2993–3007. https://doi.org/10.1088/0953-4075/35/13/312

[13] Krishnakumar, E., and Srivastava, S. K., "Ionization Cross Sections of Rare-Gas Atoms by Electron Impact," *Journal of Physics B: Atomic, Molecular and Optical Physics*, Vol. 21, No. 6, 1988, pp. 1055–1082. https://doi.org/10.1088/0953-4075/21/6/014

[14] Ichihara, D., Uchigashima, A., Iwakawa, A., and Sasoh, A., "Electrostatic Ion Acceleration across a Diverging Magnetic Field," *Applied Physics Letters*, Vol. 109, No. 5, 2016, Paper 053901. https://doi.org/10.1063/1.4960363

[15] Ichihara, D., and Sasoh, A., "Similar Thrust Performance in Diverging-Magnetic-Field Electrostatic Thruster with Monoatomic Propellants," *Journal of Propulsion and Power*, Vol. 35, No. 1, 2019, pp. 236–238. https://doi.org/10.2514/1.B37294

[16] Ichihara, D., Iwakawa, A., and Sasoh, A., "Effects of Magnetic Field Profile Near Anode on Ion Acceleration Characteristics of a Diverging Magnetic Field Electrostatic Thruster," *Journal of Applied Physics*, Vol. 122, No. 4, 2017, Paper 043302. https://doi.org/10.1063/1.4995286

[17] Sasoh, A., and Arakawa, Y., "A High-Resolution Thrust Stand for Ground Tests of Low-Thrust Space Propulsion Devices," *Review of Scientific Instruments*, Vol. 64, No. 3, 1993, pp. 719–723. https://doi.org/10.1063/1.1144204

[18] Ichihara, D., Uno, T., Kataoka, H., Jeong, J., Iwakawa, A., and Sasoh, A., "Ten-Ampere-Level, Applied-Field-Dominant Operation in Magnetoplasmadynamic Thrusters," *Journal of Propulsion and Power*, Vol. 33, No. 2, 2017, pp. 360–369. https://doi.org/10.2514/1.B36179

[19] Walker, M. L. R., Hofer, R. R., and Gallimore, A. D., "Ion Collection in Hall Thrusters Plumes," *Journal of Propulsion and Power*, Vol. 22, No. 1, 2006, pp. 205–209. https://doi.org/10.2514/1.11953

[20] Brown, D. L., Larson, C. W., Beal, B. E., and Gallimore, A. D., "Methodology and Historical Perspective of a Hall Thruster Efficiency Analysis," *Journal of Propulsion and Power*, Vol. 25, No. 6, 2009, pp. 1163–1177. https://doi.org/10.2514/1.38092

[21] Simpson, J. A., "Design of Retarding Field Energy Analyzers," *Review of Scientific Instruments*, Vol. 32, No. 12, 1961, pp. 1283–1293. https://doi.org/10.1063/1.1717235

[22] Chabert, P., and Braithwaite, N., *Physics of Radio-Frequency Plasmas*, Cambridge Univ. Press, Cambridge, England, U.K., 2011, pp. 348–353. https://doi.org/10.1017/CBO9780511974342

[23] Johnson, E. O., and Malter, L., "A Floating Double Probe Method for Measurements in Gas Discharge," *Physical Review*, Vol. 80, No. 1, 1950, pp. 58–68. https://doi.org/10.1103/PhysRev.80.58

[24] Fruchtman, A., Zoler, D., and Makrinich, G., "Potential of an Emissive Cylindrical Probe in Plasma," *Physical Review E*, Vol. 84, No. 2, 2011, Paper 025402. https://doi.org/10.1103/PhysRevE.84.025402

[25] Snyder, J. S., Lenguito, G., Frieman, J. D., Haag, T. W., and Mackey, J. A., "The Effects pf Background Pressure on SPT-140 Thruster Performance at Multiple Power Levels," *2018 Joint Propulsion Conference*, AIAA Paper 2018-4421, Cincinnati, OH, 2018. https://doi.org/10.2514/6.2018-4421

[26] Yamasaki, J., Yokota, S., and Shimamura, K., "Performance Enhancement of an Argon-Based Propellant in a Hall Thruter," *Vacuum*, Vol. 167, Sept. 2019, pp. 520–523. https://doi.org/10.1016/j.vacuum.2018.09.042

[27] Shabshelowitz, A., Gallimore, A. D., and Peterson, P. Y., "Performance of a Helicon Hall Thruster Operating with Xenon, Argon, and Nitrogen," *Journal of Propulsion and Power*, Vol. 30, No. 3, 2014, pp. 664–671. https://doi.org/10.2514/1.B35041

[28] Fujita, D., Kawashima, R., Ito, Y., Akagi, S., Suzuki, J., Schönherr, T., Koizumi, H., and Komurasaki, K., "Operating Parameters and Oscillation Characteristics of an Anode-Layer Hall Thruster with Argon Propellant," *Vacuum*, Vol. 110, Dec. 2014, pp. 159–164. https://doi.org/10.1016/j.vacuum.2014.07.022

[29] Charles, C., Boswell, R. W., and Lieberman, M. A., "Xenon Ion Beam Characterization in a Helicon Double Layer Thruster," *Applied Physics Letters*, Vol. 89, No. 26, 2006, Paper 261503. https://doi.org/10.1063/1.2426881

[30] Yu, D., Hu, P., Liu, H., and Shen, Y., "Experimental Study on the Ionization Regions in a Multi-Cusped Field Thruster," *Plasma Source Science and Technology*, Vol. 27, No. 7, 2018, Paper 075012. https://doi.org/10.1088/1361-6595/aac961

[31] Lieberman, M. A., and Lichtenberg, A. J., *Principles of Plasma Discharges and Materials Processing*, 2nd ed., Wiley, Hoboken, NJ, 2005, p. 302. https://doi.org/10.1002/0471724254

[32] Wilbur, P. J., and Kaufman, H. R., "Double Ion Production in Argon and Xenon Ion Thrusters," *Journal of Spacecraft and Rockets*, Vol. 16, No. 4, 1979, pp. 264–267. https://doi.org/10.2514/3.57654

G. G. Spanjers
Associate Editor

Queries

1. AU: Please check that the copyright (©) type is correct. Please note that the code will be added upon publication.
2. AU: The sentence “Snyder et al. [25] reported the effect of background pressure on . . . ” is not clear. Please check.
3. AU: The sentence “Regardless of B, F, and J_d increased with increasing $\dot{m}_a$” is not clear. Please check.
4. AU: Please expand KAKENHI.
5. AU: Please provide publisher’s name and location for Ref. [7].

Funding Information

The following research funding sources have been associated with your manuscript:

- Japan Society for the Promotion of Science; Award no. 18H03813;
  Funder ID http://dx.doi.org/10.13039/501100001691

Funding sources listed here can be 1) research grants from outside agencies or organizations or 2) if an author is employed by a U.S. government agency that directly funded this research, this employer also may be listed here as a funding agency. Please confirm that this information is complete and correct for all authors. Edit the Funding Data/Acknowledgments section of your paper if you have changes to funding agency names or grant numbers. Use the funder’s full and official name.